Gourd-shaped hole array germanium (Ge)-on-insulator photodiodes with improved responsivity and specific detectivity at 1,550 nm

BONGKWON SON,[1,4] (iD) HAO ZHOU,[1] (iD) YIDING LIN,[1,2,3] (iD) KWANG HONG LEE,[2] (iD) AND CHUAN SENG TAN[1,2,5]

[1] *School of Electrical and Electronic Engineering, Nanyang Technological University, 50 Nanyang Avenue, 639798, Singapore*
[2] *Low Energy Electronic Systems (LEES), Singapore-MIT Alliance for Research and Technology (SMART), 138602, Singapore*
[3] *Currently with the Max Planck Institute of Microstructure Physics, Halle (Saale), 06120, Germany*
[4] *BONGKWON001@e.ntu.edu.sg*
[5] *TanCS@ntu.edu.sg*

Abstract: Gourd-shaped hole array germanium (Ge) vertical *p-i-n* photodiodes were designed and demonstrated on a germanium-on-insulator (GOI) substrate with the excellent responsivity of 0.74 A/W and specific detectivity of 3.1×10^{10} cm·Hz$^{1/2}$/W. It is calculated that the gourd-shaped hole design provides a higher optical absorption compared to a cylinder-shaped hole design. As a result, the external quantum efficiency for the gourd-shaped hole array photodetector was enhanced by ∼2.5× at 1,550 nm, comparing with hole-free array photodetectors. In addition, the extracted specific detectivity is superior to that of commercial bulk Ge photodiodes. The 3-dB bandwidth for the hole array photodetectors is improved by ∼10% due to a lower device capacitance. This work paves the way for low-cost and high-performance CMOS compatible photodetectors for Si-based photonic-integrated circuits.

1. Introduction

Group-IV semiconductor materials besides silicon (Si) have been attractive in photonic integrated circuits (PICs) for their low cost and high compatibility in integration with complementary metal-oxide-semiconductor (CMOS) circuits. In near-infrared (NIR) range, germanium (Ge) and silicon-germanium (SiGe) alloys have been adopted to compensate for the weak optical absorption of Si [1,2]. Besides, Ge has been considered as a promising material for electronics and spintronics due to its excellent carrier mobility [3,4]. Such advantages of the widely applicable Ge material properties have been used for the NIR range sensing and optical communications integrated with CMOS circuits [5].

Ge has been broadly utilized in demonstrating the essential PIC components, i.e., a laser, a waveguide, a modulator, and a photodetector [6–10]. Among them, numerous Ge photodetectors have been introduced and developed in the past years as a key optical device in the front end of a receiver to convert the optical signal to the electronic one [11–16]. However, current industrial markets have been dominated by III-V compound photodetectors to integrate with Si-based semiconductor chips due to high responsivity and low dark leakage current. Despite the remarkable III-V photodetector performances, the cost-effectiveness and CMOS compatibility desire the Ge photodetector back to be the optical receiver for Si-based PIC.

The previously demonstrated Ge photodetectors have suffered from low responsivity [10,11]. In general, a thick *i*-Ge layer or incorporating with Sn enhances optical absorption [17,18]. However, it brings up an increase in the dark current density, resulting from the Shockley Read Hall (SRH) and Trap-assisted Tunneling (TAT) leakages mechanisms [19]. Also, the thick

i-Ge layer blocks further bandwidth improvement due to the long transit time of photo-excited electron-hole pairs (EHPs). Photon-trapping microstructures and the dual-absorption structure were introduced to improve optical absorption and frequency response [20–22]. Although the normal-incidence Ge photodiodes provide excellent responsivitiy (∼0.91 A/W) and 3dB bandwidth (4.14 GHz), it displays a high dark current density, degrading specific detectivity (*D**). For the photon-trapping structures, the dark current density even increases with the hole array fill factors due to the surface area enhancement [22]. This increase would be expected to be more critical to epi-Ge with low defect density.

As described above, an epitaxial Ge photodetector on Si substrate or on Si-on-insulator platforms suffers from a prominent dark current, originated from the high interface defects between Ge and Si [23]. A germanium-on-insulator (GOI) platform is an alternative platform to eliminate the interface defective regions [24]. Additional oxygen (O$_2$)-anneal process on the GOI platform reduced amount of threading dislocation density (TDD), being suitable for the sub-mA/cm^2 dark current density [11]. As TDD decreases to below ∼10^7 cm^{-2}, the surface leakage current mainly becomes the main contributer for the total leakage current, especially for a photodetector with a diameter of <100 μm [25].

In this paper, the gourd-shaped hole array *p-i-n* photodetectors were fabricated on the annealed GOI platform. The dark current density is enhanced by 16 to 61% as the fill factors increase from 6 to 28%, thanks to the GeO$_x$ surface passivation and the superior epi-Ge quality. It is simulated that the gourd-shaped hole array structures display higher optical absorption, comparing to the cylinder-shaped hole array structures. Responsivity is obtained to be 0.74 A/W at 1,550 nm of wavelength, which enhances external quantum efficiency (*EQE*) by ∼150%. Specific detectivity (*D**) is obtained to be 3.1 × 10^{10} cm·A/W, at 1,550 nm wavelength, comparable with the commercial Ge/extended-InGaAs photodetectors. The 3dB bandwidth is enhanced by ∼10%, resulting from a low capacitance. The high responsivity and considerable *D** for the groud-shaped hole array Ge vertical *p-i-n* photodetector pave the way toward high-efficiency photodetectors for Si-based photonics.

2. Photodetector design and fabrication

The GOI fabrication is described as follows. A Ge layer was grown on a 6" Si substrate via a metal-organic chemical vapor deposition (MOCVD) reactor. Boron (B) ion implantation was performed on the top of Ge to form *p*$^+$-Ge. Insulator layers, SiO$_2$ and SiN, were deposited on another Si and the epi-Ge wafers. The epi-Ge wafer was flipped over on the other Si wafer, and the wafer pairs were then subject to bond in N$_2$ ambient. After the bonding, the Si donor layer on the bonded wafer was etched by tetramethylammonium hydroxide (TMAH) solution, followed by chemical-mechanical polishing (CMP) process. Note that the *p*$^+$-Ge region is located in the bottom of epi-Ge after the bonding process. Subsequently, O$_2$ annealing was conducted for 4 hrs at 750°C to alleviate the number of defective regions in epi-Ge, followed by a diluted HF solution etching [26,27]. Etch pit density (EPD) was measured as ∼10^6 cm^{-2} in the annealed GOI [19]. It should be noted that going through the O$_2$ annealing process, threading dislocation density (TDD) was reduced by two orders of magnitudes, as described in Ref. 21. The cross-sectional transmission electron microscope (TEM) image for annealed GOI is shown in Fig. 1(a). The epi-Ge layer with a thickness of 1.2 μm is located above the insulator platform of SiO$_2$/SiN/SiO$_2$. Inset in Fig. 1(a) displays the high-resolution TEM (HRTEM) image of the zoom-in region of the red square in Fig. 1(a), showing a uniform and high-quality crystallinity. High-resolution X-ray diffraction (HRXRD) for epi-Ge before and after the bonding/O$_2$ annealing processes shows in Fig. 1(b). The epi-Ge peak of the annealed-GOI platform is shifted to Ge bulk compared to Ge on Si, meaning that the strain is relaxed. The estimated strain for the annealed GOI is 0.07% of the biaxial strain. The epi-Ge curve after the bonding is more symmetric than that of Ge on Si, implying the intermediate SiGe layer is mostly removed. Vertical *p-i-n* Ge structures

of the annealed-GOI platform were completed after P (Phosphorus) ion implantation, followed by the annealing process to activate the dopants. Figure 1(c) displays a spreading resistance profile (SRP) for the vertical *p-i-n* GOI structure. The n^+- and p^+-regions are formed in the top and bottom of epi-Ge, respectively. Thanks to the high dose implantation to epi-Ge, the doping concentrations of n^+- and p^+-regions are 5×10^{18} cm^{-3} and 5×10^{19} cm^{-3} in narrow regions. The *i*-Ge width was obtained as ~150 nm.
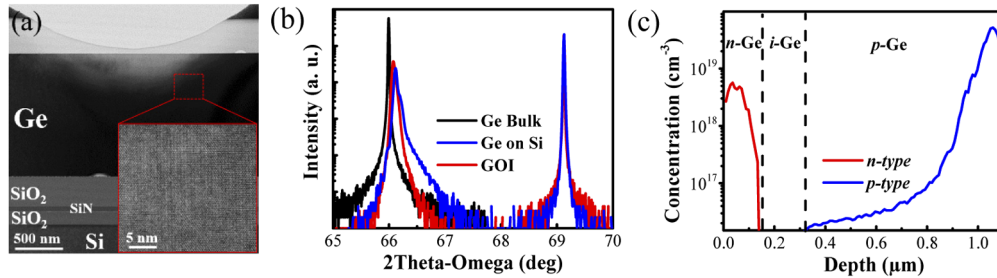

Fig. 1. (a) The cross-sectional transmission electron microscope (TEM) image of the annealed germanium-on-insulator (GOI) platform. Inset represents the high-resolution TEM (HRTEM) image of the annealed epi-Ge layer. (b) HRXRD (004) $2\theta - \omega$ scan of annealed GOI with bulk Ge and epi-Ge before the bonding process. (c) SRP profiles of B and P in the annealed-Ge vertical *p-i-n* structure.

In photodetector fabrication, the electron-beam lithography (EBL) was firstly conducted to define hole array structure patterns on the annealed-GOI platform. For the EBl process, the dose and the voltage should be properly defined to avoid damage on a sample or either overexposure or underexposure. The *n*- and *p*-Ge mesas were then defined with the device diameters of 60, 80, 150, and 250 μm by SF$_6$-based inductively coupled plasma ion etching (ICP-RIE) for the isotropic etching. The annealed-GOI surface was then cleaned via a buffered oxide etching (BOE) process. Subsequently, the deposition of a 1nm Al$_2$O$_3$ layer was conducted with atomic layer deposition (ALD), and the O$_3$ oxidation was performed at room temperature for 20 min. An additional SiO$_2$ passivation layer was then deposited on epi-Ge via plasma-enhanced chemical vapor deposition (PECVD). The BOE process was performed to expose the metal contact area by etching SiO$_2$/Al$_2$O$_3$/GeO$_x$ of the insulator layers. The metal contact was performed with Ti/TiN/Al by sputtering. A lift-off process completes photodetector fabrication, followed by rapid thermal annealing (RTA) at 400°C to enhance ohmic contact between Ge and metal. The higher annealing temperature could increase the Ohmic resistance between metal/Ge [28,29]. The planar SEM image for the completed hole array vertical *p-i-n* photodetector with a 250 μm diameter on the GOI platform is displayed in Fig. 2(a). The hole array structure was formed at the center region of the photodetector, and the central electrode is connected to the top *n*-Ge area, while both bottom electrodes are linked with the *p*-Ge area. The inset in Fig. 2(a) shows the zoom-in image of the hole structure region in the red-squared region in Fig. 2(a). The three-dimensional (3D) schematic illustration of the hole structured-Ge photodetector is shown in Fig. 2(b). It should be noted that the thin Al$_2$O$_3$/GeO$_x$ layers exist on epi-Ge for excellent surface passivation.

Figure 3(a) represents the cross-section image of TEM analysis for hole array structures for the photodetector. The hole arrays were designed with the period and diameter of 1.55 and 1.06 μm, respectively. The gourd-shaped hole design was demonstrated via the isotropic etching process. Only the ~600 nm top layer was etched down during the etching process. Figure 3(b) displays the HRTEM image of Al$_2$O$_3$/GeO$_x$ interface layers on the sidewall. The thickness of Al$_2$O$_3$/GeO$_x$ is ~3 nm, indicating that the thin GeO$_x$ surface layer was successfully formed via the room-temperature O$_3$ oxidation process [11,30].
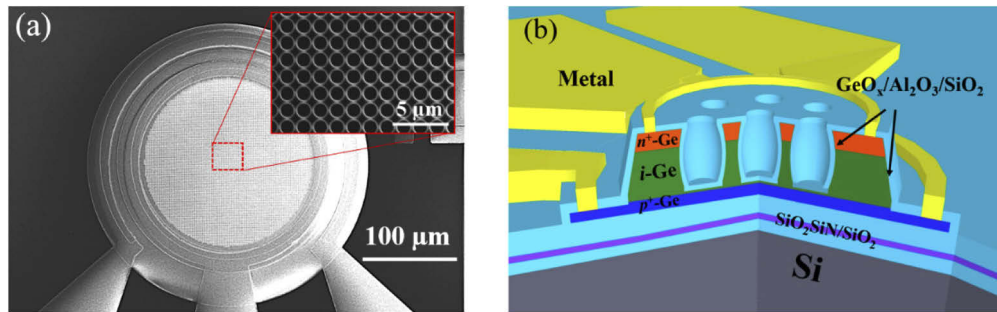
Fig. 2. (a) Top view SEM image of the hole array Ge vertical *p-i-n* photodetector with a 250 µm diameter. Inset shows the zoom-in SEM image of the hole array structure. (b) Three-dimensional (3D) schematic image of the gourd-shaped hole array Ge vertical *p-i-n* photodetector.
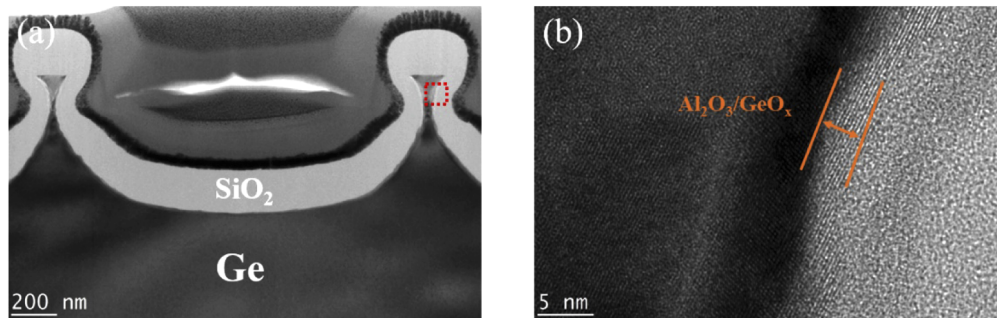

Fig. 3. (a) The cross-sectional TEM image of the gourd-shaped hole array photodetector. (b) The HRTEM image of GeO_x/Al_2O_3 layers for the red-squared region in Fig. 3(a).

3. Photodetector characterizations

3.1. Gourd-shaped hole array structure design and analysis

The GOI platform's electric field density was calculated with and without hole array structures using the finite-difference time-domain (FDTD) method, considering a periodic boundary condition. The polarization dependence was not considered owing to the round shape of the holes. For the calculation, the window size is defined to be 1.55 µm × 1.55 µm × 9.00 µm, and the time step is 0.028 fs. The mesh with a 1.30 µm × 1.30 µm × 2.00 µm size is applied in the hole structures. Figure 4(a) and (d) display the cross-sectional and top views of the calculated electric field density distribution in the simple GOI platform, respectively, at the wavelength of 1,550 nm. The distributed electrical field shows constructive and destructive interference patterns vertically in the GOI platform [31]. Figure 4(b) and (e) show the cross-sectional and top views of the electric field density distribution, respectively, in the cylinder-shaped hole array structure with a period of 1.55 µm and a diameter of 1.16 µm. For the hole array Ge structures, the lateral propagation of incoming light was observed along with the vertical propagation. It should be noted that the electrical field in the cylinder-shaped hole array structures is enhanced. This improvement results from that the hole array structures manipulate the direction of the incoming photons. The induced lateral resonance mode makes the light trapped in hole arrays for a relatively long time, leading to high optical absorption [32]. Figure 4(c) and (f) represent the cross-sectional and top views of electric field density distribution, respectively, in the gourd-shaped hole array structure. The high electric field distribution is observed in the active region. The electric field

intensity in the gourd-shaped hole is improved, comparing with the cylinder-shaped hole array design. It is worth noting that the top view for the gourd-shaped hole region displays higher electric field distribution than the cylinder-shaped hole region as calculated in Fig. 4(e) and (f). It has been reported that the nanocone structure causes whispering gallery modes, enhancing the photoresponse [33]. Also, it provides low surface reflectance by gradually increasing the diameter of the structure from top to bottom. The hourglass-shaped structure benefits from the multiple optical mode generation and the photon-trapping phenomenon, contributed by the upper and bottom parts of the hourglass-shaped hole structure, respectively [34]. As such, the gourd-shaped hole design provides high optical absorption due to the low surface reflectance and enhanced optical confinement in the hole regions. The calculated refletnace for the gourd-shaped hole was reduced by ~2.6× in comparison with the one for the cylinder-shaped hole.
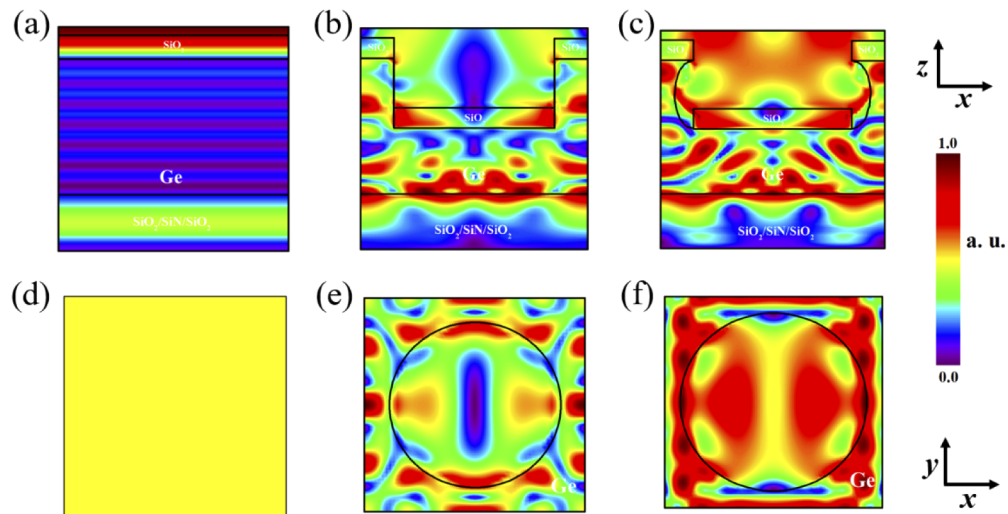

Fig. 4. (a) Cross-sectional and (d) top views of electric field distribution (E_x) in the GOI platform. (b) Cross-sectional and (e) top views of electric field distribution in the GOI platform with the cylinder-shaped hole array structure. (c) Cross-sectional and (f) top views of electric field distribution in the GOI platform with the gourd-shaped hole array structure. The simulated area is a unit cell of each structure. The selected wavelength for the FDTD simulation is 1,550 nm.

The absorption spectra were calculated using reflectance and transmission extracted from the FDTD simulation in Fig. 5(a). It should be noted that all the absorption for the hole array designs is improved, comparing to the hole-free array one due to the lateral propagation of the incoming photons. In the various hole designs, the gourd-shaped hole array shows high optical absorption caused by the multiple modes generation in the gourd-shaped hole regions. It is worth noting that the high absorption spectra sustain beyond the Ge bandgap, implying the cut-off wavelength extension. Since the hole period and the hole diameter are the important parameters to determine the optical absorption, the various gourd-shaped hole array conditions are optimized accordingly in Fig. 5(b). The optimized diameter and period conditions are 1.16 and 1.55 µm, respectively, providing ~75% optical absorption at 1,550 nm wavelength.

3.2. Demonstration and performances for gourd-shaped hole array photodetector

The photocurrent was measured using a tunable laser operating in the wavelength range of 1,500 to 1,630 nm. The incident light from a single-mode optical fiber is illuminated on the central top region of photodetectors. The output optical power coupled out from the single-mode
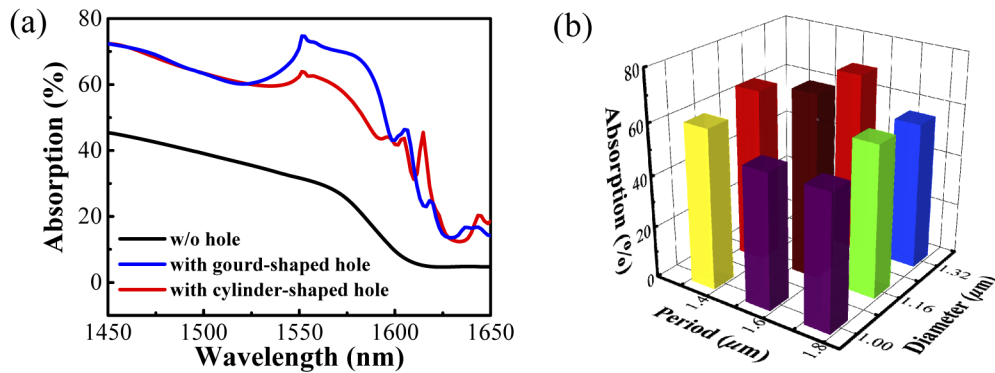
Fig. 5. (a) The absorption spectra for the gourd-shaped and cylinder-shaped hole array structures in the wavelength range of 1,500 to 1,650 nm, comparing with the hole-free array structures. (b) Calculated absorption at 1,550 nm wavelength, comparing with various gourd-shaped hole array designs in terms of period and diameter of gourd-shaped hole array.

optical fiber was calibrated to be 0.4 mW consistently in the overall wavelength range using the fiber optic power meter (ILX Lightwave FPM-8220). Figure 6(a) illustrates the photo- (I_{photo}) and dark-current (I_{dark}) as a function of voltage at the wavelength of 1,550 nm. I_{photo} for the hole array photodetector is higher than that of the hole-free photodetector. It should be noted that, as calculated in Fig. 5, I_{photo} for the hole array photodetector is improved due to the optical confinement enhancement in the hole array structures. Various hole array structures were fabricated, considering the unexpected fabrication process results in terms of micro-loading effect, non-uniform SiO_2 surface passivation, and so on. The optical absorption efficiency can be determined by the external quantum efficiency (EQE). EQE can be obtained by the following equation,

$$EQE = \frac{hc}{e\lambda}R \quad (1)$$

where h, c, e, and λ are Planck's constant, the velocity of the light, the electronic charge, and the excitation wavelength, respectively. Figure 6(b) shows EQE with respect to various hole periods and diameters. EQE for all the hole array photodetectors is larger than 28%, EQE for the hole-free photodetector. It should be noted that the hole array structure with a 1.55 µm period and a 1.08 µm diameter provides 70% EQE, enhanced by 2.5 fold.

Figure 7(a) and (b) represent the responsivity scanning for the hole array photodetector with various period and diameter conditions with respect to wavelength from 1,500 to 1,630 nm. Figure 7(a) represents the responsivity scanning for photodetectors with varying diameter conditions and the fixed period of 1.50 µm. The hole array photodetectors show higher responsivity in the overall wavelength range than the hole-free array photodetector. As the hole diameter size increases, the cut-off wavelength is extended. Figure 7(b) displays the responsivity scanning for photodetectors with varying period conditions and the fixed diameter of 1.16 µm. As the period is reduced, the cut-off wavelength is extended. As the period reaches 1.50 µm, the maximum responsivity of 0.74 A/W was obtained at 1,550 nm wavelength. It is observed that the variation in period condition provides a relatively large variation of responsivity comparing to Fig. 7(a), meaning the hole array structure design is mainly affected by the period condition. The responsivity can be further enhanced by increasing the i-Ge thickness.

Figure 8(a) displays the I_{dark}-V curve comparison between photodetectors with and without the hole array structures. Fill factor (FF) can be obtained by FF = *hole area/mesa area* [22]. The photodetectors with 6 and 28% of FF increase I_{dark} by ~16 and ~61%, respectively. It has been reported that the fill factor of ~20% for the hole array photodetector enhances J_{dark} by
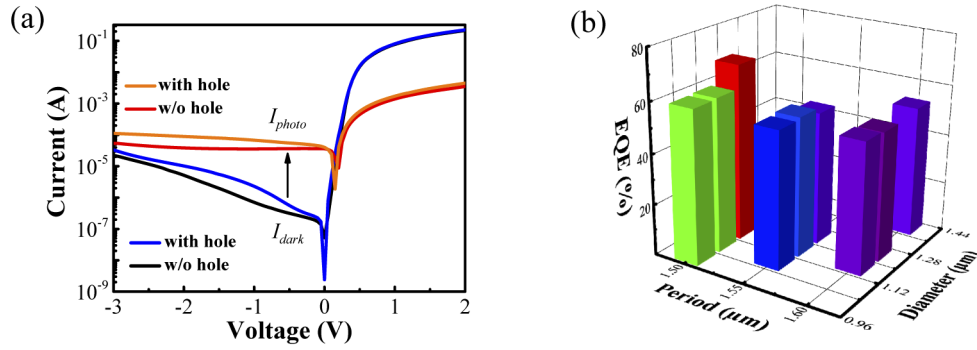
Fig. 6. (a) Photocurrent of a vertical *p-i-n* photodetector with and without the gourd-shaped hole array structure. The arrow represents the photocurrent generation under illumination. (b) EQE at 1,550 nm wavelength for the gourd-shaped hole array Ge photodetectors as a function of hole diameters and period.
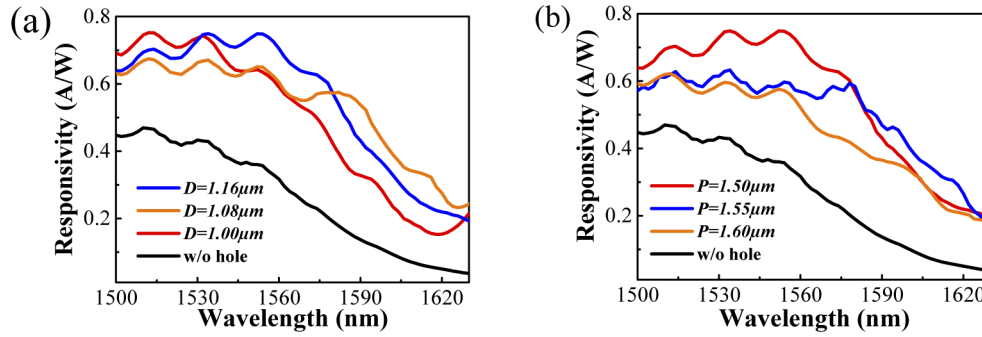

Fig. 7. Optical responsivity spectra for the gourd-shaped hole array photodetectors with varying (a) diameters from 1.00 to 1.16 μm and (b) the period from 1.50 to 1.60 μm conditions as a function of wavelength from 1,500 to 1,630 nm under -1 V. The responsivity spectra for the hole-free array photodetector are also displayed.

~600% [22]. The following two approaches are considered for suppressing J_{dark} in the hole array structure. The epi-Ge is only etched down for ~600nm, leaving ~600nm of the epi-Ge layer at the bottom. Additionally, the surface is passivated by GeO_x. The combination of the two approaches contributes to suppressing J_{dark} in the hole array structure. J_{dark} for photodetectors with and without the hole array structure is displayed in Fig. 8(b) as a function of applied reverse bias from 0 to −5 V in the increasing temperature from 293 to 353 K. J_{dark} for the hole array photodetector was 1.41 mA/cm² at 293 K, increasing by ~20%. *FF* for temperature-dependent photodetectors is calculated to be 8%. Dark current can be further reduced by reducing the misfit dislocation and TDD. It has been reported that ~100× reduction on TDD reduced the dark current by ~53× [19].

To further study the dark leakage current generation, the Arrhenius plot was extracted in Fig. 9(a) for the hole array photodetector in the applied voltage range of −0.1 to −5V. The slopes become flat by increasing reverse bias voltage, meaning that the temperature barely affects the I_{dark} variation at relatively high reverse bias voltage. The following equation can obtain the activation energy (E_a),

$$\ln\left(\frac{I_{dark}}{T^{1.5}}\right) = -\frac{E_a}{kT} + \ln(A) \tag{2}$$
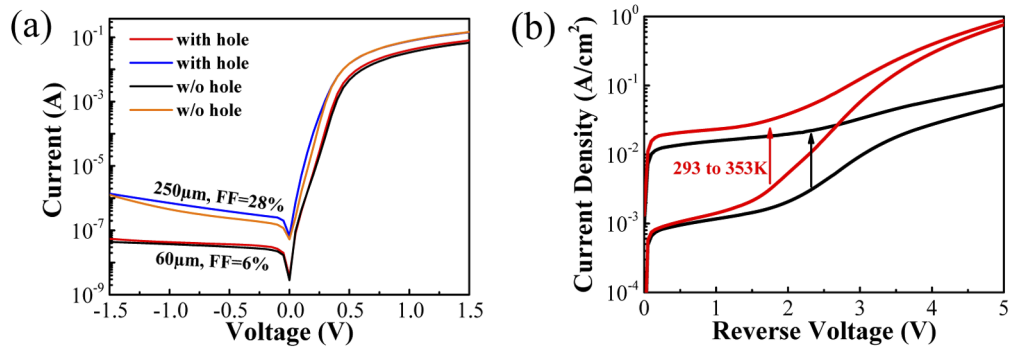
Fig. 8. (a) I_{dark}-V curves for photodetectors with and without gourd-shaped hole array structures. The fill factor of 6 and 28% are corresponding to 60 and 250 μm diameter photodetectors, respectively, and are compared with the hole-free array ones. (b) Elevating current characteristics of photodetectors with and without the gourd-shaped hole array structures as a function of reverse voltage from 0 to −5 V under varying temperatures from 293 to 353 K.

where k, T, and A are temperature, a constant, and the Boltzmann constant. The extracted E_a is shown in Fig. 9(b) along with the hole-free array one. Overall, E_a for the hole array photodetector is varied from 0.5 to ∼0.0 eV. At low reverse bias, E_a is high, signifying the leakage current is sensitive to the change in temperature. As the reverse voltage goes high, on the other hand, the leakage current is insensitive to the temperature variation. This agrees well with the observations in our prior work [19]. In general, at the relatively high reverse voltage, the electric field in epi-Ge is enhanced, leading to the enhancement in the tunneling leakage current mechanisms, i.e., TAT and band-to-band tunneling (BTBT). Hence, E_a can be ∼0 eV since the TAT, BTBT leakages are barely dependent on the elevating temperature. It should be noted that the hole array structures improve the tunneling leakage current at the high reverse voltage (Fig. 9(b)).
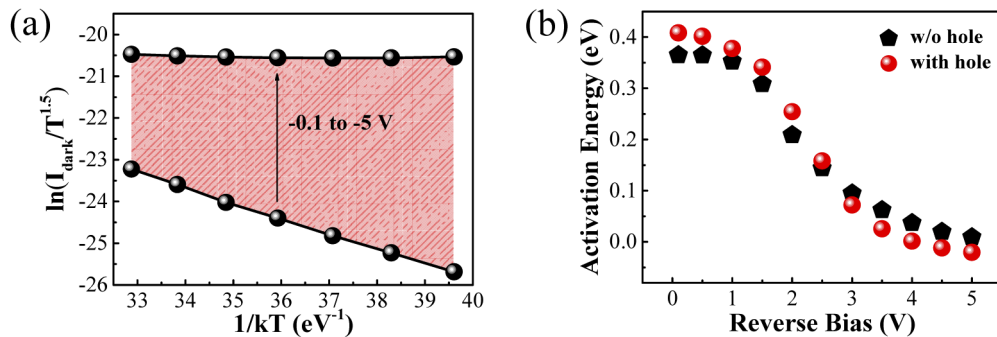

Fig. 9. (a) Arrhenius plot for the gourd-shaped hole array photodetector with the varying temperature range from 293 to 353 K. The arrow indicates the increase in the voltage from −0.1 to −5.0 V. (b) Activation energy of the hole and the hole-free photodetector at a function of reverse bias from −0.1 to −0.5 V.

The measured responsivity for the hole array Ge photodetector is benchmarked comparing with the reported normal incidence Ge photodetectors with respect to dark leakage current density at −1 V in Fig. 10. Ge photodetectors on various substrate platforms were compared, such as a Si substrate platform, a GOI platform with and without the hole array structures, and a silicon-on-insulator (SOI) platform with and without the hole array structures. For the case of the

Si substrate platform, the increase in the thickness of epi-Ge shows relatively high responsivity. However, such a thick thickness of the intrinsic Ge layer causes high dark current density by enhancing SRH and TAT leakage mechanisms. Besides, it limits bandwidth by the restricted transit 3-dB bandwidth. By inserting the insulator layer underneath, i.e., GOI and Si-on-insulator (SOI) platforms, the responsivity is further enhanced, although the photodetectors contain the thin *i*-Ge layer. This improvement is because the insulator layer makes the photons stay relatively long in the active area, which originated from the high optical confinement in the active region. Recently, the hole array structures have been introduced in the micro-and nano-size scales [22,37]. By doing so, the responsivity up to 0.91 A/W was achieved utilizing the SOI platforms. However, despite the excellent responsivity, J_{dark} is still high in the level of > 20 mA/cm^2. Such dark current restricts the further improvement on the specific detectivity D^*, which is a leading figure of merit to characterize photodetector performance in various materials. In this work, the hole array Ge photodetectors on the GOI platform were demonstrated. J_{dark} is significantly low in the level of ~1mA/cm^2 due to the superior epi-Ge quality and the GeO$_x$ surface passivation [42], maintaining high responsivity of 0.74A/W due to the gourd-shaped hole array design. It should be noted that the responsivity for the demonstrated hole array photodetector is remarkable, considering a thin *i*-Ge layer of 288 nm at −1 V.
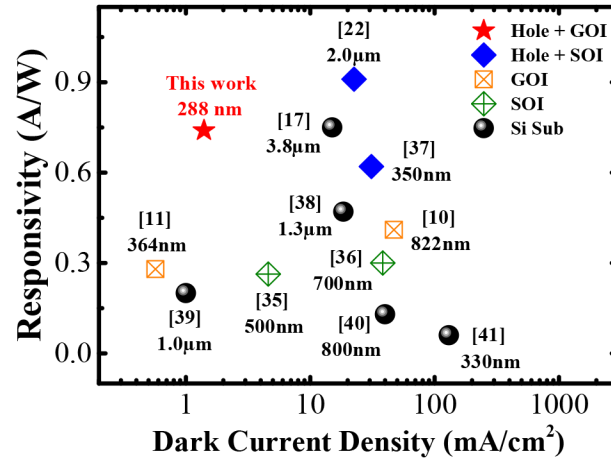

Fig. 10. Benchmarking of responsivities for normal incidence epi-Ge vertical photodetectors with respect to dark current density using various platforms, i. e., the SOI platform with and without hole array structures, the GOI platform with and without hole array structures, and the Si substrate platform [10,11,17,35–41]. The responsivity at 1,550 nm wavelength displays for dark current density at −1 V. The *i*-Ge thicknesses are indicated below the Ref. numbers.

Specific detectivity (D^*) can be extracted by [43]

$$D^* = \frac{R\sqrt{A\Delta f}}{I_{rms}} \tag{3}$$

where A is the mesa size for a photodetector, Δf is the noise bandwidth, and I_{rms} is the root-mean-square noise current. I_{rms} can be obtained by two dominant components, thermal noise ($I_{thermal}$) and shot noise (I_{shot}). The I_{rms} can be expressed as follow,

$$I_{rms} = \sqrt{I_{thermal}^2 + I_{shot}^2} \tag{4}$$

$$I_{thermal} = \sqrt{4kT\Delta f/R_{shunt}} \tag{5}$$

$$I_{shot} = \sqrt{2qI_{dark}\Delta f} \qquad (6)$$

where R_{shunt} is shunt resistance for a photodetector. Δf is assumed to be 1 Hz. R_{shunt} can be extracted by providing the first derivative of V to I_{dark} near 0V. The extracted R_{shunt} for photodetectors with and without the hole array structure is 1.7 and 1.9 MΩ, respectively. Low R_{shunt} for the hole array one results from the increase in the dark leakage current. The calculated $I_{thermal}$ displays 9.8×10^{-14} and 9.3×10^{-14} A·Hz$^{-1/2}$ for photodetectors with and without the hole array structure, respectively. I_{shot} is obtained to be 1.39 and 1.38×10^{-13} A·Hz$^{-1/2}$ for the photodetectors with and without hole array structure, respectively. D^* for the hole array photodetector is extracted to be 3.1×10^{10} cm·Hz$^{1/2}$/W, at the 1,550 nm wavelength, which is improved by ~1.5×, compared with the hole-free array one. The D^* spectra in the wavelength range from 1,500 to 1,630 nm were compared with that of the commercial Ge/extended-InGaAs photodetectors in Fig. 11 [44,45]. The D^* spectra for the hole array photodetector are sustained at the order of 10^{10} cm·Hz$^{1/2}$/W beyond 1,600 nm. In addition, it should be noted that the hole array photodetector shows ~10× D^* enhancement at 1,600 nm due to the cut-off wavelength extension.
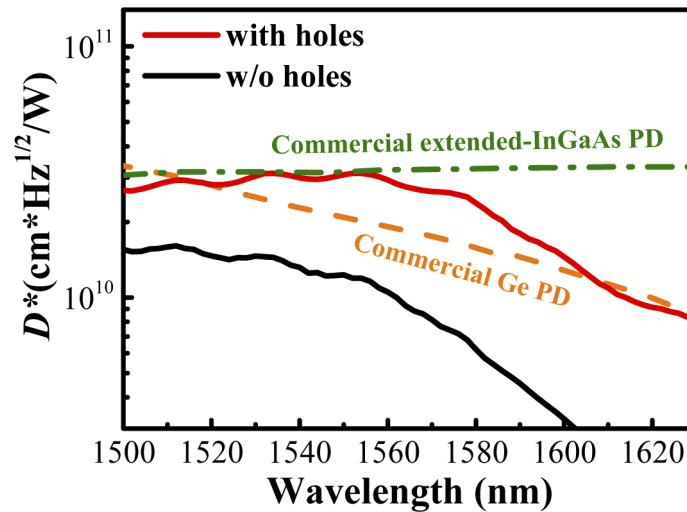

Fig. 11. The specific detectivity D^* spectrum of the gourd-shaped hole array vertical *p-i-n* photodetector with respect to the wavelength from 1,500 to 1,630 nm in comparison with the hole-free array Ge photodetector at a reverse bias of −1 V. D^* for commercial Ge and extended-InGaAs photodetectors also displays as Refs. [44].

The 3dB bandwidth of the hole array photodetector on the GOI platform was performed with frequency measurement capability up to 20 GHz in Fig. 12(a). The illumination wavelength of 1,550 nm was selected for the 3dB bandwidth experiment. The 3dB bandwidth for the hole array photodetector with a 150 µm diameter was 0.50 GHz at −5 V. The 3 dB bandwidth is improved by ~10% at −5 V by designing the hole array structure [18]. Voltage-dependent 3dB bandwidth for the hole array photodetectors is shown in Fig. 12(b). At low applied voltage, no noticeable change for the bandwidth between the photodetectors with and without the hole array structure was observed. As the reverse bias increases beyond −1 V, it shows a noticeable difference between them. In addition, the 3 dB bandwidth is improved with a smaller mesa diameter and an increase in reverse bias voltage, implying that RC-limited delay mainly dominates the bandwidth.

Figure 13(a) represents the *C-V* measurement for photodetectors with and without the hole array structure. The capacitance for the one with the hole array shows a similar tendency at low reverse bias voltage. At high reverse voltage, a capacitance gap between with and without
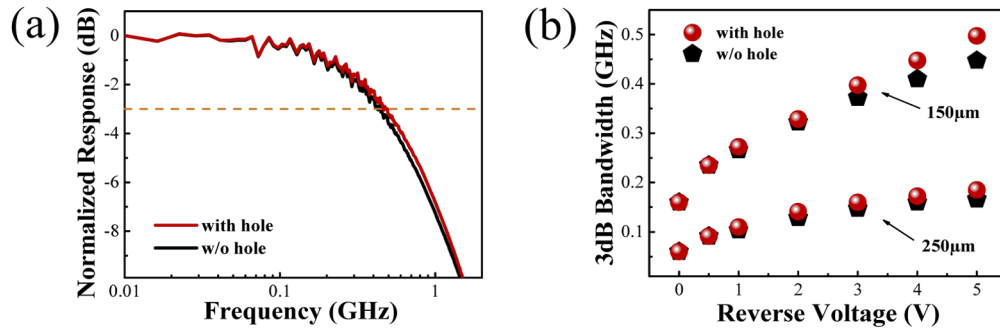
Fig. 12. (a) 3 dB bandwidth measurement of the gourd-shaped hole array photodetectors with a diameter of 150 μm on the GOI platform at the incident wavelength of 1,550 nm under −5 V in comparison with the one without the hole array. (b) 3 dB bandwidth as a function of reverse bias from 0 to −5 V, compared with the one without the hole array with varying photodetector mesa sizes of 150 and 250 μm diameters.

the hole array structure is distinguishable. Depletion width (d) can be extracted by the linear regression of capacitance against the mesa area based on the equation of $d = \varepsilon A/C_j$, where A and C_j are the mesa area and junction capacitance, respectively. The inset in Fig. 13(b) represents capacitances as a function of mesa areas. d is extracted to be ~150 nm at 0 V and increases up to ~600 nm at −5 V. C_j can be separated into hole area capacitance ($C_{j,hole}$) and hole-free area capacitance ($C_{j,no-hole}$) as shown in the inset in Fig. 13(a). At low reverse voltage, $C_{j,hole}$ is mainly attributed to device capacitance. Considering the fact that the depletion width increases with reverse voltage, $C_{j,no-hole}$ contributes to the capacitance as the reverse bias voltage increases. As a result, the total capacitance is reduced, leading to the high 3dB bandwidth at high reverse voltage. It should be noted that a smaller mesa area for the photodetectors is expected to improve the bandwidth by reducing the RC-limited bandwidth [11].
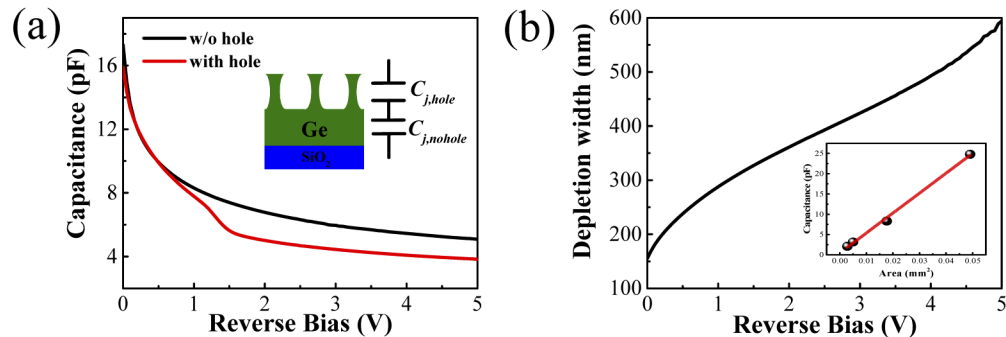

Fig. 13. (a) C-V measurement for photodetectors with and without the gourd-shaped hole array structure as a function of reverse voltage from 0 to −5 V. The inset of the schematic image displays the cross-sectional view of a hole array structure and the corresponding capacitances. (b) Extracted depletion width as a function of reverse bias. Inset displays the capacitance with varying mesa areas at −1 V.

4. Conclusion

The gourd-shaped hole array Ge *p-i-n* photodiodes were designed and demonstrated on the GOI substrate. The hole array structures were designed via the FDTD simulation, and the

photodetectors were fabricated accordingly. It was simulated that the gourd-shaped hole array design displays high optical absorption compared to that of the cylinder-shaped hole array design. As a result, the responsivity for the gourd-shaped hole array photodetector was 0.74 A/W at 1,550 nm along with low J_{dark} of 1.4 mA/cm^2 at -1 V. The combination of the insulating platform and the ground-shaped hole array design improves the responsivity by $\sim 2.5 \times$. The specific detectivity D^* was extracted to be 3.1×10^{10} cm·Hz$^{1/2}$/W at 1,550 nm wavelength. The 3dB bandwidth for the hole array photodetector increased by 10% under -5 V due to the low capacitance. Therefore, these devices are potentially well-suited for low-cost and high-performance CMOS compatible photodetectors for Si-based photonic-integrated circuits.

References

1. K. H. Lee, S. Bao, Y. Lin, W. Li, P. Anantha, L. Zhang, Y. Wang, J. Michel, E. A. Fitzgerald, and C. S. Tan, "Hetero-epitaxy of high quality germanium film on silicon substrate for optoelectronic integrated circuit applications," J. Mater. Res. **32**(21), 4025–4040 (2017).
2. J.-M. Fèdèli, P. Labeye, A. Marchant, O. Lartigue, M. Fournier, and J. M. Hartmann, "Ge/SiGe photonic devices for the long mid-infrared," *Proc. SPIE 10686, Silicon Photonics: From Fundamental Research to Manufacturing*, 106860M (2018).
3. P. S. Goley and M. K. Hudait, "Germanium Based Field-Effect Transistor Challenges and Opportunities," Materials **7**(3), 2301–2339 (2014).
4. N. W. Hendrickx, D. P. Franke, A. Sammak, G. Scappucci, and M. Veldhorst, "Fast two-qubit logic with holes in germanium," Nature **577**(7791), 487–491 (2020).
5. C. V. Poulton, A. Yaacobi, D. B. Cole, M. J. Byrd, M. Raval, D. Vermeulen, and M. R. Watts, "Coherent solid-state LIDAR with silicon photonic optical phased arrays," Opt. Lett. **42**(20), 4091–4094 (2017).
6. W. Li, P. Anantha, K. H. Lee, H. D. Qiu, X. Guo, S. C. K. Goh, L. Zhang, H. wang, R. A. Soref, and C. S. Tan, "Spiral Waveguides on Germanium-on-Silicon Nitride Platform for Mid-IR Sensing Applications," IEEE Photonics J. **10**(3), 1–7 (2018).
7. S. Bao, D. Kim, C. Onwukaeme, S. Gupta, K. Saraswat, K. H. Lee, Y. Kim, D. Min, Y. Jung, H. Qiu, H. Wang, E. A. Fitzgerald, C. S. Tan, and D. Nam, "Low-threshold optically pumped lasing in highly strained germanium nanowire," Nat. Commun. **8**(1), 1845 (2017).
8. W. Li, P. Anantha, S. Bao, K. G. Lee, X. Guo, T. Hu, L. Zhang, H. Wang, R. Soref, and C. S. Tan, "Germanium-on-silicon nitride waveguides for mid-infrared integrated photonics," Appl. Phys. Lett. **109**(24), 241101 (2016).
9. S. A. Srinivasan, M. Pantouvaki, S. Gupta, H. Y. Chen, P. Verheyen, G. Lepage, G. Roelkens, K. Saraswat, D. V. Thourhout, P. Absil, and J. V. Campenhout, "56 Gb/s Germanium Waveguide Electro-Absorption Modulator," J. Lightwave Technol. **34**(2), 419–424 (2016).
10. Y. Lin, K. Lee, S. Bao, X. Guo, H. Wang, J. Michel, and C. S. Tan, "High-efficiency normal-incidence vertical p-i-n photodetectors on a germanium-on-insulator platform," Photonics Res. **5**(6), 702–709 (2017).
11. B. Son, Y. Lin, K. H. Lee, Y. Wang, S. Wu, and C. S. Tan, "High speed and ultra-low dark current Ge vertical p-i-n photodetectors on an oxygen-annealed Ge-on-insulator platform with GeO$_x$ surface passivation," Opt. Express **28**(16), 23978–23990 (2020).
12. H. T. Chen, P. Verheyen, P. De Heyn, G. Lepage, J. De Coster, P. Absil, G. Roelkens, and J. Van Campenhout, "High-Responsivity Low-Voltage 28-Gb/s Ge p-i-n Photodetector With Silicon Contacts," J. Lightwave Technol. **33**(4), 820–824 (2015).
13. D. Benedikovic, L. Virot, G. Aubin, F. Amar, B. Szelag, B. Karakus, J.-M. Hartmann, C. Alonso-Ramos, X. L. Roux, P. Crozat, E. Cassan, D. Marris-Morini, C. Baudot, F. Boueuf, J.-M. Fédéli, C. Kopp, and L. Vivien, "25 Gbps low-voltage hetero-structured silicon-germanium waveguide pin photodetectors for monolithic on-chip nanophotonic architectures," Phot. Res. **7**(4), 437–444 (2019).
14. D. Benedikovic, L. Virot, G. Aubin, J.-M. Hartmann, F. Amar, B. Szelag, X. Le Roux, C. Alonso-Ramos, P. Crozat, É. Cassan, D. Marris-Morini, C. Baudot, F. Boeuf, J.-M. Fédéli, C. Kopp, and L. Vivien, "Comprehensive Study on Chip-Integrated Germanium Pin Photodetectors for Energy-Efficient Silicon Interconnects," IEEE J. Quantum Electron. **56**(1), 1–9 (2020).
15. H. Chen, P. Verheyen, P. De Heyn, G. Lepage, J. De Coster, S. Balakrishnan, P. Absil, W. Yao, L. Shen, G. Roelkens, and J. Van Campenhout, "-1 V bias 67 GHz bandwidth Si-contacted germanium waveguide p-i-n photodetector for optical links at 56 Gbps and beyond," Opt. Express **24**(5), 4622–4631 (2016).
16. D. Benedikovic, L. Virot, G. Aubin, J.-M. Hartmann, F. Amar, X. Le Roux, C. Alonso-Ramos, É. Cassan, D. Marris-Morini, J.-M. Fédéli, F. Boeuf, B. Szelag, and L. Vivien, "Silicon-germanium receivers for short-wave-infrared optoelectronics and communications," Nanophotonics **10**(3), 1059–1079 (2021).

17. S. Famà, L. Colace, G. Masini, and G. Assanto, "High performance germanium-on-silicon detectors for optical communications," Appl. Phys. Lett. **81**(4), 586–588 (2002).

18. H. Zhou, S. Xu, Y. Lin, Y.-C. Huang, B. Son, Q. Chen, X. Guo, K. H. Lee, S. C.-K. Goh, X. Gong, and C. S. Tan, "High-efficiency GeSn/Ge multiple-quantum-well photodetectors with photon-trapping microstructures operating at 2μm," Opt. Express **28**(7), 10280–10293 (2020).

19. B. Son, Y. Lin, K. H. Lee, Q. Chen, and C. S. Tan, "Dark Current Analysis of Germanium-oninsulator Vertical p-i-n Photodetectors with Varying Threading Dislocation Density," J. Appl. Phys. **127**(20), 203105 (2020).

20. Y. Gao, H. C. Ansizoglu, K. G. Polat, S. Ghandiparsi, A. Kaya, H. H. Mamtaz, A. S. Mayet, Y. Wang, X. Zhang, T. Yamada, E. P. Devine, A. F. Elrefair, S.-Y. Wang, and M. S. Islam, "Photon-trapping microstructures enable high-speed high-efficiency silicon photodiodes," Nat. Photonics **11**(5), 301–308 (2017).

21. X. Li, L. Peng, Z. Liu, X. Liu, J. Zheng, Y. Zuo, C. Xue, and B. Cheng, "High-power back-to-back dual-absorption germanium photodetector," Opt. Lett. **45**(6), 1358–1361 (2020).

22. H. Cansizoglu, C. Bartolo-Perez, Y. Gao, E. P. Devine, S. Ghandiparsi, K. G. Polat, H. H. Mamtax, T. Yamada, A. F. Elrefaie, S.-Y. Wang, and M. S. Islam, "Surface-illuminated photon-trapping high-speed Ge-on-Si photodiodes with improved efficiency up to 1700 nm," Photonics Res. **6**(7), 734–742 (2018).

23. B. Son, Y. Lin, K. H. Lee, and C. S. Tan, "Dark Current Analysis of Vertical p-i-n Photodetectors on a Germanium-on-Insulator Platform," *2019 IEEE 16th International Conference on Group IV Photonics (GFP)*, 1–2 (2019).

24. Y. Wang, B. Wang, D. F. S. Eow, J. Michel, K. E. K. Lee, S. F. Yoon, E. A. Fitzgerald, C. S. Tan, and K. H. Lee, "Performance of AlGaInP LEDs on silicon substrates through low threading dislocation density (TDD) germanium buffer layer," Semicond. Sci. Technol. **33**(10), 104004 (2018).

25. T. H. Loh, H. S. Nguyen, R. Murthy, M. B. Yu, W. Y. Loh, G. Q. Lo, N. Balasubsramanian, and D. L. Kwong, Appl. Phys. Lett. 91, 073503 (2007).

26. K. H. Lee, S. Bao, G. Y. Gong, Y. H. Tan, E. A. Fitzgerald, and C. S. Tan, "Fabrication and characterization of germanium-on-insulator through epitaxy, bonding, and layer transfer," J. Appl. Phys. **116**(10), 103506 (2014).

27. K. H. Lee, S. Bao, G. Y. Chong, Y. H. Tan, E. A. Fitzgerald, and C. S. Tan, "Defects reduction of Ge epitaxial film in a germanium-on-insulator wafer by annealing in oxygen ambient," APL Mater. **3**(1), 016102 (2015).

28. Q. Zhang, N. Wu, T. Osipowicz, L. K. Bera, and C. Zhu, "Formation and Theraml Stability of Nickel Germanide on Germanoium Substrate," Jpn. J. Appl. Phys. **44**(45), L1389–L1391 (2005).

29. S. Zhum M, B. Yu, G. Q. lo, and D. L. Kwong, "Enhanced thermal stability of nickel germanide on thin epitaxial germanium by adding an ultrathin titanium layer," Appl. Phys. Lett. **91**(5), 051905 (2007).

30. Y. Xu, G. Han, H. Liu, Y. Wang, Y. Liu, J. Ao, and Y. Hao, "Ge pMOSFETs with GeOx Passivation Formed by Ozone and Plasma Post Oxidation," Nanoscale Res. Lett. **14**(1), 126 (2019).

31. S. Ghosg, K.-C. Lin, C.-H. Tsai, K. H. Lee, Q. Chen, B. Son, B. Mukhopadhyay, C. S. Tan, and G.-E. Chang, "Resonant-cavity-enhanced responsivity in germanium-on-insulator photodetectors," Opt. Express **28**(16), 23739–23747 (2020).

32. Y. Gao, H. Cansizoglu, S. Ghandiparsi, C. Bartolo-Perez, E. P. Devine, T. Yamada, A. F. Elrefaie, S.-Y. Wang, and M. S. Islam, "High Speed Surface Iluminated Si Photodiode Using Microstructured Holes for Absorption Enhancements at 900-`000 nm Wavelength," ACS Photonics **4**(8), 2053–2060 (2017).

33. L. Zhou, X. Yu, and J. Zhu, "Metal-Core/Semiconductor-Shell Nanocones for Broadband Solar Absorption Enhancement," Nano Lett. **14**(2), 1093–1098 (2014).

34. K. Kim, S. Yoon, M. Seo, S. Lee, H. Cho, M. Meyyappan, and C.-K. Baek, "Whispering gallery modes enhance the near-infrared photoresponse of hourglass-shaped silicon nanowire photodiodes," Nat. Electron. **2**(12), 572–579 (2019).

35. Z. Liu, F. Yang, W. Wu, H. Cong, J. Zheng, C. Lu, C. Xue, B. Cheng, and Q. Wang, "48 GHz High-Performance Ge-on-SOI Photodetector With Zero-Bias 40 Gbps Grown by Selective Epitaxial Growth," J. Lightwave Technol. **35**(24), 5306–5310 (2017).

36. C. Li, C. Xue, Z. Liu, B. Cheng, C. Li, and Q. Wang, "High-Bandwidth and High-Responsivity Top-Illuminated Germanium Photodiodes for Optical Interconnection," IEEE Trans. Electron Devices **60**(3), 1183–1187 (2013).

37. J. Song, S. Yuan, C. Cui, Y. Wang, Z. Li, A. X. Wang, C. Zeng, and J. Xia, "High-efficiency and high-speed germanium photodetector enabled by multiresonant photonic crystal," Nanophotonics **3**, 1081–1087 (2021).

38. D. Suh, S. Kim, J. Joo, and G. Kim, "36-GHz High-Responsivity Ge Photodetectors Grown by RPCVD," IEEE Photonics Technol. Lett. **21**(10), 672–674 (2009).

39. L. Colace, G. Assanto, D. Fulgoni, and L. Nash, "Near-Infrared p-i-n Ge-on-Si Photodiodes for Silicon Integrated Receivers," J. Lightwave Technol. **26**(16), 2954–2959 (2008).

40. Z. Zhou, J. He, R. Wang, C. Lu, and J. Yu, "Normal incidence p-i-n Ge heterojunction photodiodes on Si substrate grown by ultrahigh vacuum chemical vapor deposition," Opt. Commun. **283**(18), 3404–3407 (2010).

41. S. Klinger, M. Berroth, M. Kaschel, M. Oehme, and E. Kasper, "Ge-on-Si p-i-n Photodiodes With a 3-dB Bandwidth of 49 GHz," IEEE Photonics Technol. Lett. **21**(13), 920–922 (2009).

42. Y. Lin, B. Son, K. H. Lee, J. Michel, and C. S. Tan, "Sub-mA/cm2 Dark Current Density, Buffer-less Germanium (Ge) Photodiodes on a 200-mm Ge-on-insulator Substrate," IEEE Trans. Electron Devices **68**(4), 1730–1737 (2021).

43. Y. Lin, K. H. Lee, B. Son, and C. S. Tan, "Low-power and high-detectivity Ge photodiodes by in-situ heavy As doping during Ge-on-Si seed layer growth," Opt. Express **29**(3), 2940–2952 (2021).

44. T. Pham, W. Du, H. Tran, J. Margetis, J. Tolle, G. Sun, R. A. Soref, H. A. Naseem, B. Li, and S.-Q. Yu, "Systematic study of Si-based GeSn photodiodes with 2.6 μm detector cutoff for short-wave infrared detection," Opt. Express **24**(5), 4519–4531 (2016).
45. C. Beskici, "Extended short wavelength infrared FPA technology: status and trends," *Proc. SPIE 10540, Quantum Sending and Nano Electronics and Photonics XV*, 105400P (2018).